

Sensitivities to New Resonance Couplings to W -Bosons at the LHC

Ying-nan Mao^{a,1}, Kechen Wang^a and Yiheng Xiong^{a,2}

^a*Department of Physics, School of Physics and Mechanics, Wuhan University of Technology, 430070 Wuhan, Hubei, China*

E-mail: ynmao@whut.edu.cn, kechen.wang@whut.edu.cn, yiheng@whut.edu.cn

ABSTRACT: We propose a search strategy at the HL-LHC for a new neutral particle X that couples to W -bosons, using the process $pp \rightarrow W^\pm X (\rightarrow W^+ W^-)$ with a tri- W -boson final state. Focusing on events with two same-sign leptonic W -boson decays into muons and a hadronically decaying W -boson, our method leverages the enhanced signal-to-background discrimination achieved through a machine-learning-based multivariate analysis. Using the heavy photophobic axion-like particle (ALP) as a benchmark, we evaluate the discovery sensitivities on both production cross section times branching ratio $\sigma(pp \rightarrow W^\pm X) \times \text{Br}(X \rightarrow W^+ W^-)$ and the coupling g_{aWW} for the particle mass over a wide range of 170–3000 GeV at the HL-LHC with center-of-mass energy $\sqrt{s} = 14$ TeV and integrated luminosity $\mathcal{L} = 3 \text{ ab}^{-1}$. Our results show significant improvements in discovery sensitivity, particularly for masses above 300 GeV, compared to existing limits derived from CMS analyses of Standard Model (SM) tri- W -boson production at $\sqrt{s} = 13$ TeV. This study demonstrates the potential of advanced selection techniques in probing the coupling of new particles to W -bosons and highlights the HL-LHC's capability to explore the physics beyond the SM.

¹Corresponding author.

²Corresponding author.

Contents

1	Introduction	1
2	The Signal Production	3
3	The SM Background	5
4	Event Simulation	5
5	Search Strategy	7
6	Results	10
7	Conclusion	11
A	Distributions of Representative Observables	12
B	Details of the MVA analyses	16
C	Distributions of BDT responses	18
D	The Selection Efficiency Table	19

1 Introduction

The search for new particles beyond the Standard Model (SM) is a cornerstone of high-energy physics, driven by unresolved questions such as the nature of dark matter, the origin of the neutrino mass, the baryogenesis, and the dark energy. Among the various extensions to the SM, new particles coupling to W -bosons represent a particularly intriguing avenue for exploration. In physics beyond the SM (BSM), there exist various types of neutral particles X which couple to W -bosons. Examples include: (i) extended gauge models with additional gauge bosons (Z') [1], which couples to W^+W^- via mixing with SM gauge bosons γ or Z ; (ii) extended scalar sectors like the Two-Higgs-Doublet Model (2HDM) [2] and supersymmetric models [3], where the new CP-even scalar couple to W^+W^- via the mixing with the SM Higgs boson, and it may also be related to some recent hints at LHC [4]; (iii) pseudo-scalars, such as axions [5–9] or axion-like particles (ALPs) a , which couple to W^+W^- via a dimension-five operator $aW_{\mu\nu}^+\widetilde{W}^{-,\mu\nu}$. Besides, new neutral particles coupling to W -bosons also emerge in theoretical frameworks such as composite Higgs models [10], extra-dimensional scenarios [11], and dark matter models [12].

Since the new neutral particle X couples to di- W -bosons, it can be produced and decay via the X - W - W vertex at the Large Hadron Collider (LHC). In this study, we consider X

produced in association with a W -boson through the s -channel exchange of a $W^{(*)}$ boson, followed by its decay into a W^+W^- pair, resulting in a tri- W -boson final state. The mass of X is assumed to be greater than 170 GeV, ensuring its di- W -boson decay products are both on-shell. We choose the heavy photophobic ALP [13] as a benchmark model in this work.

Axion models were originally proposed to address the strong CP problem in QCD [9, 14]. In these models, the axion arises as a pseudo-Nambu-Goldstone boson from a spontaneously broken $U(1)$ symmetry at a high energy scale, a mechanism known as the Peccei-Quinn mechanism [5, 6]. In such original models [5–8, 15–21], couplings of the axion is strictly related to its mass m_a . For the extended concept of ALPs, the mass and couplings of ALPs are treated as independent parameters. This flexibility significantly broadens the ALP parameter space, making them promising candidates for astrophysical and collider-based searches [22–24]. At colliders, ALPs are typically studied through their interactions with SM particles [25–35]. Among these interactions, previous experiments have primarily focused on the ALP’s coupling to diphoton, $g_{a\gamma\gamma}$. The constraints on $g_{a\gamma\gamma}$ are stringent across most of the ALP mass range, with limits coming from astrophysical phenomena for $m_a \lesssim \mathcal{O}(\text{MeV})$ [36, 37], low-energy e^-e^+ collisions for $0.1 \text{ GeV} \lesssim m_a \lesssim 10 \text{ GeV}$ [38–40], Pb-Pb collisions at the LHC for $10 \text{ GeV} \lesssim m_a \lesssim 100 \text{ GeV}$ [41, 42], and p - p collisions at the LHC for $100 \text{ GeV} \lesssim m_a \lesssim 2 \text{ TeV}$ [29]. Consequently, the ALP-photon coupling is expected to be small, motivating the study of photophobic ALPs [13]. Photophobic ALPs are characterized by suppressed couplings to diphoton, with their primary interactions occurring with other SM electroweak bosons.

Previous studies [13, 43, 44] on heavy photophobic ALPs at the LHC have derived limits based on tri- W -boson final state by reinterpreting experimental analyses at center-of-mass energy $\sqrt{s} = 8$ or 13 TeV, with limited luminosities and mass ranges. Ref. [13] derives constraints on ALP masses in the range of 40 – 500 GeV by reinterpreting triboson searches in the SM framework at $\sqrt{s} = 8 \text{ TeV}$, where the ATLAS analyses of $pp \rightarrow W^\pm(\rightarrow \mu^\pm\nu) W^\pm(\rightarrow \mu^\pm\nu) W^\mp(\rightarrow jj)$ with $\mathcal{L} = 20.3 \text{ fb}^{-1}$ [45] were utilized as a ALP-mediated signal process $pp \rightarrow W^\pm a(\rightarrow W^\pm W^\mp)$. Ref. [43] reinterprets the CMS analyses of the SM process $pp \rightarrow jj W^\pm(\rightarrow \ell^\pm\nu) W^\pm(\rightarrow \ell^\pm\nu)$ at $\sqrt{s} = 13 \text{ TeV}$ [46] as a non-resonant ALP-mediated vector boson scattering process, with the ALP serving as an off-shell mediator, and the results reveal discovery sensitivities for a photophobic ALP with a mass below 100 GeV at the High-Luminosity LHC (HL-LHC) with $\sqrt{s} = 14 \text{ TeV}$ and $\mathcal{L} = 3 \text{ ab}^{-1}$. Ref. [44] reinterpreted the CMS analyses for SM process $pp \rightarrow W^\pm W^\pm W^\mp$ at $\sqrt{s} = 13 \text{ TeV}$ with $\mathcal{L} = 35.9 \text{ fb}^{-1}$ [47] as a ALP-mediated signal process $pp \rightarrow W^\pm a(\rightarrow W^\pm W^\mp)$, setting limits on ALP mass up to 1 TeV.

More recently, some of our authors conducted detailed analyses of the γZ decay mode for heavy photophobic ALPs at the HL-LHC with $\sqrt{s} = 14 \text{ TeV}$ [48]. In that study, ALPs are produced with two jets through s -channel vector boson exchange and vector boson fusion, resulting in the process $pp \rightarrow jj a(\rightarrow \gamma Z(\rightarrow \ell^+\ell^-))$, where $\ell = e, \mu$. Machine-learning-based multivariate analyses were used to optimize background rejection. Discovery sensitivities for the ALP coupling to di- W -bosons, g_{aWW} , were evaluated over masses from 100 to 4000 GeV with $\mathcal{L} = 3 \text{ ab}^{-1}$ and 140 fb^{-1} . Other studies on heavy photophobic ALPs

at the LHC are also reviewed in Ref. [48]. Besides, heavy photophobic ALPs have also been studied through a global fit analysis of electroweak precision observables [49].

We note that since the referred experimental analyses were designed to target SM production processes, rather than the heavy photophobic ALPs, discrepancies in signal kinematics and background characteristics frequently result in conservative or potentially unreliable discovery sensitivities for previous reinterpreting studies. In this study, we accomplish detailed analyses and derive discovery sensitivities at the HL-LHC for a new heavy neutral particle X that couples to W -bosons, using the process $pp \rightarrow W^\pm X (\rightarrow W^+ W^-)$ with a tri- W -boson final state. Compared with previous reinterpreting studies based on tri- W -boson final state, key advancements include: (i) performing simulations for signal process of $pp \rightarrow W^\pm X (\rightarrow W^+ W^-)$ and related background processes to fully capture signal and background kinematics at the detector-level; (ii) using machine learning-based multivariate analysis (MVA) for optimal signal-to-background discrimination; (iii) presenting results over a wide mass range $170 - 3000$ GeV at $\sqrt{s} = 14$ TeV with $\mathcal{L} = 3 \text{ ab}^{-1}$; (iv) providing the model-independent discovery sensitivities for the production cross section times branching ratio, $\sigma(pp \rightarrow W^\pm X) \times \text{Br}(X \rightarrow W^+ W^-)$, which can be applied to general models involving a new heavy neutral particle X that couples to W -bosons.

This paper is organized as follows. In Sec. 2, we introduce the signal process under study. Sec. 3 outlines the main SM backgrounds relevant to our signal. In Sec. 4 and Sec. 5, we describe the simulation setup and search strategy, respectively. Our results are presented in Sec. 6, and we conclude in Sec. 7. Additional details supporting the main text are provided in the appendices.

2 The Signal Production

As shown in Fig. 1, we consider the production of X in association with a W -boson at the HL-LHC with center-of-mass energy $\sqrt{s} = 14$ TeV. X then decays to di- W boson. The corresponding signal process is $pp \rightarrow W^\pm X (\rightarrow W^+ W^-)$, leading to the tri- W -boson final state. To eliminate the background effectively, two same charged W -bosons are required to decay leptonically into muons, leading to the existence of same-sign muons in the final state. The remanent W -boson decays hadronically to di-jet which has larger branching ratio and can increase the signal production cross section.

To accomplish a concrete study, in this work, we take the ALP theory model as an example. The neutral particle X is assumed to be the heavy photophobic ALP which couples to electroweak gauge bosons only. The effective linear ALP Lagrangian is [50]

$$\mathcal{L}_{\text{eff}} \supset \frac{1}{2} (\partial_\mu a) (\partial^\mu a) - \frac{1}{2} m_a^2 a^2 - c_{\tilde{W}} \frac{a}{f_a} W_{\mu\nu}^b \tilde{W}^{b,\mu\nu} - c_{\tilde{B}} \frac{a}{f_a} B_{\mu\nu} \tilde{B}^{\mu\nu}, \quad (2.1)$$

where $W_{\mu\nu}^b$ and $B_{\mu\nu}$ represent the field strength tensors of the $\text{SU}(2)_L$ and $\text{U}(1)_Y$ gauge groups, and $\tilde{O}^{\mu\nu} \equiv \frac{1}{2} \epsilon^{\mu\nu\alpha\beta} O_{\alpha\beta}$ ($O = W, B$) is the dual field strength tensor. m_a and f_a denote the mass of ALP and its decay constant¹, respectively, and they are assumed to be

¹In ALP models, f_a always affects on physical observables together with the coefficients c_i [such as the coefficients $c_{\tilde{W}, \tilde{B}}$ in Eq. (2.1)], thus people can only set constraints on the combinations c_i/f_a . As a new physics scale, f_a is expected to be much higher than the electro-weak scale, thus we expect $f_a \gtrsim \mathcal{O}(\text{TeV})$.

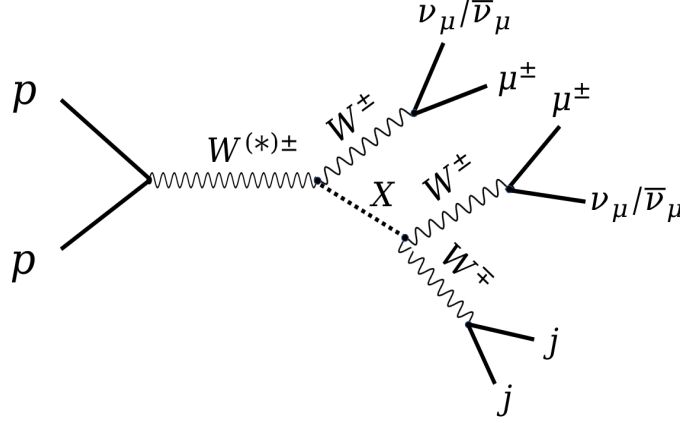


Figure 1: Production and decay of new particle X coupling to di- W boson at pp colliders, leading to the tri- W final state. The same-charged W^\pm bosons are considered to decay into μ^\pm and ν_μ (or $\bar{\nu}_\mu$), while the remaining W^\mp boson decays into di-jet.

independent parameters in this work.

After electroweak symmetry breaking, the interactions between ALP and gauge bosons are generally expressed as

$$\begin{aligned} \mathcal{L}_{\text{eff}} \supset & -\frac{1}{4} g_{a\gamma\gamma} a F_{\mu\nu} \tilde{F}^{\mu\nu} - \frac{1}{2} g_{a\gamma Z} a Z_{\mu\nu} \tilde{F}^{\mu\nu} \\ & - \frac{1}{4} g_{aZZ} a Z_{\mu\nu} \tilde{Z}^{\mu\nu} - \frac{1}{2} g_{aWW} a W_{\mu\nu}^+ \tilde{W}^{-,\mu\nu}, \end{aligned} \quad (2.2)$$

where $F_{\mu\nu}$, $Z_{\mu\nu}$ and $W_{\mu\nu}^+$ are the field strength tensors of the electromagnetic field, Z - and W -fields. In addition, the coupling constants are expressed as

$$\begin{aligned} g_{a\gamma\gamma} &= \frac{4}{f_a} (s_\theta^2 c_{\tilde{W}} + c_\theta^2 c_{\tilde{B}}), \\ g_{aZZ} &= \frac{4}{f_a} (c_\theta^2 c_{\tilde{W}} + s_\theta^2 c_{\tilde{B}}), \\ g_{a\gamma Z} &= \frac{2 s_{2\theta}}{f_a} (c_{\tilde{W}} - c_{\tilde{B}}), \\ g_{aWW} &= \frac{4}{f_a} c_{\tilde{W}}, \end{aligned} \quad (2.3)$$

where $c_{\tilde{W}}$ and $c_{\tilde{B}}$ are the same constants in Eq. (2.1), and $c_\theta = \cos \theta_W$, $s_\theta = \sin \theta_W$, $s_{2\theta} = \sin 2\theta_W$ are all trigonometric functions of the Weinberg angle θ_W . In this work, focusing on the photophobic ALP scenario, we assume the coupling between ALP and diphoton $g_{a\gamma\gamma} = \frac{4}{f_a} (s_\theta^2 c_{\tilde{W}} + c_\theta^2 c_{\tilde{B}}) = 0$. As a consequence, $s_\theta^2 c_{\tilde{W}} + c_\theta^2 c_{\tilde{B}} = 0$, making a constant proportional relationship between $c_{\tilde{W}}$ and $c_{\tilde{B}}$. Thus, $g_{a\gamma Z}$ and g_{aZZ} can be expressed as functions of g_{aWW} :

$$g_{a\gamma Z} = t_\theta g_{aWW}, \quad \text{and} \quad g_{aZZ} = (1 - t_\theta^2) g_{aWW}, \quad (2.4)$$

where $t_\theta = \tan \theta_W$.

3 The SM Background

Since the signal final state contains two same-sign muons plus di-jet and moderate missing energy, relevant SM processes which can mimic the signal are listed as follows,

- (i) one-boson production with two jets: $W^\pm jj$ and Zjj ;
- (ii) two-boson production with two jets: $W^\pm W^\pm jj$, $W^+ W^- jj$, $W^\pm Zjj$ and $ZZjj$;
- (iii) three-boson production: $W^\pm W^\pm W^\mp$;
- (iv) top quark pair production: $t\bar{t}$.

After W -boson decays, the processes $W^\pm W^\pm jj$ and $W^\pm W^\pm W^\mp$ can result in the same final state as the signal and serve as irreducible backgrounds, despite their relatively low production cross sections. The process $W^\pm jj$, which has a significantly higher production cross section, also contributes to the background due to the potential misidentification of muons. Additionally, charge mis-measurement of final state muons can lead to backgrounds from processes like Zjj , $W^+ W^- jj$, and $t\bar{t}$. Furthermore, the $W^\pm Zjj$ process becomes relevant when one of the muons in the final state remains undetected, and the $ZZjj$ process can contribute both through missed muons and mis-measured muon charges.

4 Event Simulation

We firstly use MadGraph5_aMC@NLO program with version 2.6.7 [51] to simulate the proton-proton collision events at the parton level where the NNPDF23 parton distribution function (PDF) [52] of the proton is utilized. At the parton level, to produce data as close to the experimental results as possible, following relatively loose thresholds are applied for both the signal and background processes: (a) the minimal transverse momentum of jets, photons and charged leptons is set to 0.5 GeV, i.e. $p_T(j/\gamma/l^\pm) > 0.5$ GeV; (b) the maximal pseudorapidity of jets is set to 10, i.e. $|\eta(j)| < 10$, and it is set to 5 for the photons and charged leptons, i.e. $|\eta(\gamma/l^\pm)| < 5$; (c) the solid angular difference $\Delta R = \sqrt{\Delta\eta^2 + \Delta\phi^2}$ between objects is set to 0.1. These thresholds criteria are set in the “run_card.dat” file of the MadGraph program.

All signal and background events are then passed through PYTHIA program with version 8.2 [53] for parton showering, hadronization and decay of unstable particles. Besides, we use the Delphes program with version 3.4.2 [54] to perform the detector simulation where the ATLAS detector configuration is adopted and the minimal transverse momenta of leptons and photons accepted by the detector is set to be 2 GeV. Due to limited computing resources, when simulating background processes of $W^\pm jj$, Zjj and $W^\pm W^\mp jj$, decay mode of one gauge boson is fixed to decay to the muon, i.e. $W^\pm(\rightarrow \mu^\pm \nu_\mu) jj$, $Z(\rightarrow \mu^+ \mu^-) jj$ and $W^\pm(\rightarrow \mu^\pm \nu_\mu) W^\mp jj$, respectively, so that these processes can still have enough number of events after all selection criteria.

For the signal, we apply the ALP model file with the linear Lagrangian [50] in the Universal FeynRules Output (UFO) format [55] into the MadGraph5 program and generate

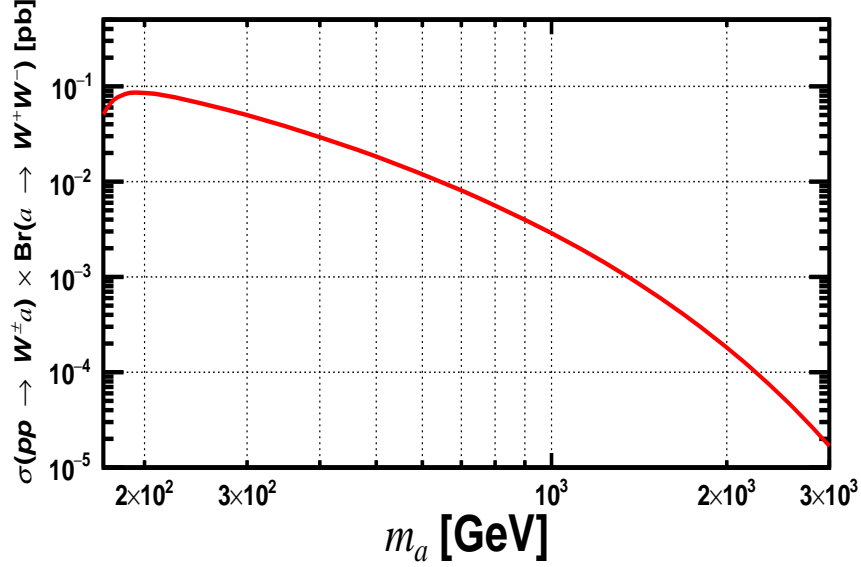


Figure 2: Signal production cross section $\sigma(pp \rightarrow W^\pm a)$ multiplied by the branching ratio $\text{Br}(a \rightarrow W^+ W^-)$ as a function of ALP mass m_a from 170 GeV to 3000 GeV at the HL-LHC with $\sqrt{s} = 14$ TeV, assuming the coupling $g_{aWW} = 1 \text{ TeV}^{-1}$.

the $pp \rightarrow W^\pm a(\rightarrow W^+ W^-)$ events. A scan of the ALP mass, m_a , is done in the following fashion: individual mass 170 GeV, 25 GeV increments in the mass range 200-300 GeV, 100 GeV increments in the mass range 300-600 GeV, individual mass 750 GeV, 800 GeV, 900 GeV, and 400 GeV increments in the mass range 1000-3000 GeV. For each ALP mass, the coupling g_{aWW} is set to 1 TeV^{-1} . For each iteration of ALP mass m_a , at least 10^6 events have been generated to ensure that statistical uncertainties are minimized as much as possible within the bounds of computational resources.

To ensure consistency in our analysis, we use the production cross sections calculated by MadGraph5 program to estimate the event yields for both signal and background processes. Figure 2 illustrates the signal production cross section $\sigma(pp \rightarrow W^\pm a)$, multiplied by the branching ratio $\text{Br}(a \rightarrow W^+ W^-)$, as a function of the ALP mass m_a in the range of 170 GeV to 3000 GeV at the HL-LHC with $\sqrt{s} = 14$ TeV, where the coupling g_{aWW} is fixed to 1 TeV^{-1} . As m_a increases beyond 160 GeV, the phase space for the decay mode $a \rightarrow W^+ W^-$ expands rapidly, leading to a sharp rise in the branching ratio, which reaches approximately 50% at ~ 190 GeV [48]. Beyond this point, the branching ratio increases more gradually, with only minor changes at higher masses. At the same time, production cross section for process $pp \rightarrow W^\pm a$ decreases steadily with increasing m_a . Consequently, the production cross section times branching ratio peaks when $m_a \sim 190$ GeV, just above the WW decay threshold of 160 GeV.

5 Search Strategy

Following preselection criteria have been employed before a multivariate analysis is done, where final state muons and jets are ordered based on their transverse momenta and labeled as O_i ($i = 1, 2, \dots$), with $O = \mu, j$, respectively.

- (1) Events are required to have exactly two muons, i.e. $N(\mu) = 2$.
- (2) The minimal p_T of the two muons is 10 GeV, i.e. $p_T(\mu) > 10$ GeV.
- (3) The two muons have the same charge, i.e. $\mu^\pm \mu^\pm$.
- (4) The minimal p_T of all jets is 30 GeV, i.e. $p_T(j) > 30$ GeV.
- (5) Event are required to have at least two jets, i.e. $N(j) \geq 2$, and the number of b -tagged jets are required to be zero, i.e. $N(j_b) = 0$.

	initial	(1)-(2)	(3)	(4)-(5)
$W^\pm a(\rightarrow W^\pm W^\mp)$	5.51×10^4	1.27×10^3	4.26×10^2	2.54×10^2
$W^\pm(\rightarrow \mu^\pm \nu_\mu)jj$	3.62×10^{11}	7.24×10^6	2.69×10^6	4.89×10^5
$Z(\rightarrow \mu^\pm \mu^\mp)jj$	3.31×10^{10}	1.13×10^{10}	3.33×10^5	6.67×10^4
$W^\pm W^\pm jj$	1.10×10^6	5.22×10^3	5.19×10^3	3.88×10^3
$W^\pm(\rightarrow \mu^\pm \nu_\mu)W^\mp jj$	5.05×10^8	2.43×10^7	8.81×10^3	4.53×10^3
$W^\pm Zjj$	1.03×10^9	1.42×10^7	6.17×10^5	1.99×10^5
$ZZjj$	3.10×10^8	8.42×10^6	4.32×10^4	1.55×10^4
$W^\pm W^\pm W^\mp$	3.79×10^5	5.92×10^3	1.73×10^3	8.55×10^2
$t\bar{t}$	1.79×10^9	1.22×10^7	8.71×10^4	2.91×10^4

Table 1: Expected number of events for the signal with benchmark mass $m_a = 500$ GeV and coupling $g_{aWW} = 1$ TeV $^{-1}$ and background processes after applying preselection criteria (1)-(5) sequentially at the HL-LHC with $\sqrt{s} = 14$ TeV and $\mathcal{L} = 3$ ab $^{-1}$.

Table 1 presents the expected number of events, N_{exp} , for the signal, with a benchmark mass of $m_a = 500$ GeV and coupling $g_{aWW} = 1$ TeV $^{-1}$, as well as for the background processes. Here, N_{exp} is calculated by the formula,

$$N_{\text{exp}} = \sigma_{\text{pro}} \times \mathcal{L} \times \epsilon_{\text{pre}}, \quad (5.1)$$

where σ_{pro} is the production cross section of the signal or background process; \mathcal{L} is the integrated luminosity; and ϵ_{pre} is the preselection efficiency which is evaluated based on our analyses. The numbers are shown after applying the preselection criteria (1)-(5) sequentially at the HL-LHC, with $\sqrt{s} = 14$ TeV and $\mathcal{L} = 3$ ab $^{-1}$. As shown in Table 1, after applying all preselection criteria, the number of background events for most processes is reduced by at least 10^4 -fold. Nevertheless, the total background rate remains much larger than the expected number of signal events.

After applying the preselection criteria, the Toolkit for Multivariate Analysis (TMVA) package [56] is employed to carry out a multivariate analysis (MVA), which enhances the ability to distinguish between signal and background events. The events that pass the preselection steps are then subjected to analysis using the Boosted Decision Trees (BDT) algorithm within the TMVA framework. In this process, the discrimination between signal and background is achieved by utilizing the following set of kinematic observables.

- (a) Missing transverse energy and its azimuth angle: $\cancel{E}_T, \phi(\cancel{E}_T)$.
- (b) The x, y and z -component of momentum (p_x, p_y, p_z) and energy (E) of the first two leading jets and muons: $p_x(j_1), p_y(j_1), p_z(j_1), E(j_1); p_x(j_2), p_y(j_2), p_z(j_2), E(j_2); p_x(\mu_1), p_y(\mu_1), p_z(\mu_1), E(\mu_1); p_x(\mu_2), p_y(\mu_2), p_z(\mu_2), E(\mu_2)$.
- (c) The number of charged tracks (N_{track}) and the ratio (R_E) of the hadronic versus electromagnetic energy deposited in the calorimeter cells for the first two leading jets: $N_{\text{track}}(j_1), N_{\text{track}}(j_2); R_E(j_1), R_E(j_2)$. R_E is typically greater than one for a jet.
- (d) The solid angular separation ΔR between j_1 and j_2 , the invariant mass (m) of system of $(j_1 + j_2)$, and the number (N) of jets: $\Delta R(j_1, j_2), m(j_1 + j_2), N(j)$.
- (e) Observables related to the isolation quality of muons. (i) The summed p_T of other objects excluding the muon in a $R = 0.4$ cone around the muon: $p_T^{\text{iso}}(\mu_1), p_T^{\text{iso}}(\mu_2)$, and the bigger of the two $p_{T, \text{max}}^{\text{iso}}(\mu)$. (ii) The ratio of the transverse energy in a 3×3 grid surrounding the muon to the p_T of the muon (the “etrat” in Ref. [57]), which is a percentage between 0 and 0.99: $R_{\text{grid}}(\mu_1), R_{\text{grid}}(\mu_2)$. (iii) We make all possible combination between μ_1/μ_2 and every jet, compare the ΔR and find the minimal value: $\Delta R_{\text{min}}(\mu, j)$. For well-isolated muons, $p_T^{\text{iso}}, R_{\text{grid}}$ should be small, while $\Delta R_{\text{min}}(\mu, j)$ is large.
- (f) To reconstruct the hadronically decaying W -boson (jj_W), we make all di-jet combinations and select the pair with the invariant mass closest to 80 GeV. The corresponding two jets are labeled as j_{W1} and j_{W2} sorted by their p_T . We input the following observables of these two jets: $p_x(j_{W1}), p_y(j_{W1}), p_z(j_{W1}), E(j_{W1}); p_x(j_{W2}), p_y(j_{W2}), p_z(j_{W2}), E(j_{W2}); N_{\text{track}}(j_{W1}), N_{\text{track}}(j_{W2}); R_E(j_{W1}), R_E(j_{W2}); \Delta R(j_{W1}, j_{W2}), m(j_{W1} + j_{W2})$.
- (g) The transverse mass m_T [58] of the system, that include one of muons and the missing transverse energy: $m_T(\mu_1 + \cancel{E}_T), m_T(\mu_2 + \cancel{E}_T)$. Here, the transverse mass $m_T \equiv \sqrt{(E_T^{\text{vis.}} + \cancel{E}_T)^2 - (\vec{p}_T^{\text{vis.}} + \vec{\cancel{p}}_T)^2}$, where $E_T^{\text{vis.}}$ ($\vec{p}_T^{\text{vis.}}$) is the transverse energy (momentum) of the visible object or system, while \cancel{E}_T ($\vec{\cancel{p}}_T$) is the missing transverse energy (momentum). $E_T^{\text{vis.}} = \sqrt{(\vec{p}_T^{\text{vis.}})^2 + (m^{\text{vis.}})^2}$, where $m^{\text{vis.}}$ is the invariant mass of the visible object or system. $\cancel{E}_T = |\vec{\cancel{p}}_T|$, assuming the invariant mass of the invisible object is zero.
- (h) We calculate and compare ΔR values of two combinations between the jj_W and μ_1/μ_2 . The muon with smaller (bigger) ΔR value is labeled as μ_a (μ_b). We input the minimal value $\Delta R(j_{W1} + j_{W2}, \mu_a)$ and maximal value $\Delta R(j_{W1} + j_{W2}, \mu_b)$.

- (i) The observables related to the reconstruction of the ALP mass: $m(j_{W1} + j_{W2} + \mu_a)$, $m(j_{W1} + j_{W2} + \mu_b)$; $m_T(j_{W1} + j_{W2} + \mu_a + \cancel{E}_T)$, $m_T(j_{W1} + j_{W2} + \mu_b + \cancel{E}_T)$.
- (j) The observables related to the reconstruction of the off-shell $W^{(*)\pm}$ boson: $m_T(j_{W1} + j_{W2} + \mu_a + \mu_b + \cancel{E}_T)$.

Details of the observables $N_{\text{track}}(j_i)$, $R_E(j_i)$, $R_{\text{grid}}(\mu_i)$ and $p_T^{\text{iso}}(\mu)$ can be found in [57]. The observables $N_{\text{track}}(j_i)$, $R_E(j_i)$, $R_{\text{grid}}(\mu_i)$, and $p_T^{\text{iso}}(\mu)$ are described in detail. The hadronic W -boson ($j j_W$) is reconstructed using the method described above. Appendix A presents distributions of kinematical observables after applying preselection criteria for signal and background processes at the HL-LHC with $\sqrt{s} = 14$ TeV. Among them, for m_a values below 500 GeV, the endpoint positions of the distributions for both $m(j_{W1} + j_{W2} + \mu_a)$ and $m_T(j_{W1} + j_{W2} + \mu_a + \cancel{E}_T)$ align closely with m_a ; when m_a exceeds 500 GeV, the endpoint positions of the $m_T(j_{W1} + j_{W2} + \mu_a + \cancel{E}_T)$ distribution are still related to m_a , but this phenomenon becomes less obvious. Appendix B provides detailed information about the MVA analyses performed using the TMVA package [56].

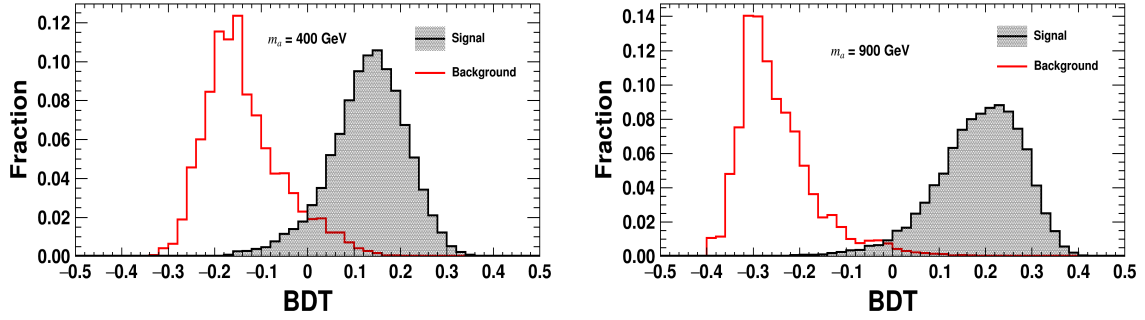


Figure 3: BDT response distributions for total SM background and the signal when ALP mass $m_a = 400$ GeV (left) and 900 GeV (right) at the HL-LHC with $\sqrt{s} = 14$ TeV.

Figure 3 presents the BDT response distributions for the total background and the signal at the HL-LHC, with benchmark masses of $m_a = 400$ GeV and $m_a = 900$ GeV. The left and right plots show similar trends in the distributions for both mass points. The clear separation between the signal and background distributions indicates that the BDT criteria are effective for background rejection at the HL-LHC. Additionally, the separation is more pronounced for $m_a = 900$ GeV compared to $m_a = 400$ GeV, suggesting improved discriminating power at higher masses. Appendix C presents distributions of BDT responses after applying preselection criteria for the signal and background processes at the HL-LHC with $\sqrt{s} = 14$ TeV, assuming various m_a cases.

After the preselection, the BDT cut is optimized according to the signal statistical significance calculated by Eq. (5.2) for each mass case.

$$\sigma_{\text{stat}} = \sqrt{2 \left[(N_s + N_b) \ln \left(1 + \frac{N_s}{N_b} \right) - N_s \right]}, \quad (5.2)$$

where N_s and N_b are the expected numbers of events for signal and total background after applying both the preselection and BDT criteria. Appendix D shows selection efficiencies of preselection and BDT criteria for signal and background processes at the HL-LHC with $\sqrt{s} = 14$ TeV assuming different ALP masses, where “–” means the number of events can be reduced to be negligible with $\mathcal{L} = 3 \text{ ab}^{-1}$.

6 Results

Using our search strategy, in Fig. 4, we present the discovery sensitivities for the production cross section $\sigma(pp \rightarrow W^\pm X)$ multiplied by the branching ratio $\text{Br}(X \rightarrow W^+ W^-)$ as a function of m_X in the mass range of 170–3000 GeV at the HL-LHC, with $\sqrt{s} = 14$ TeV and an integrated luminosity of $\mathcal{L} = 3 \text{ ab}^{-1}$. The red and green curves correspond to the 2- σ and 5- σ significances, respectively. As shown in the BDT distributions in Appendix C, the separation between the signal and background improves significantly for larger masses, leading to more effective background rejection. Consequently, the sensitivities for heavier masses do not decrease very rapidly, demonstrating strong discovery potential across a wide mass range.

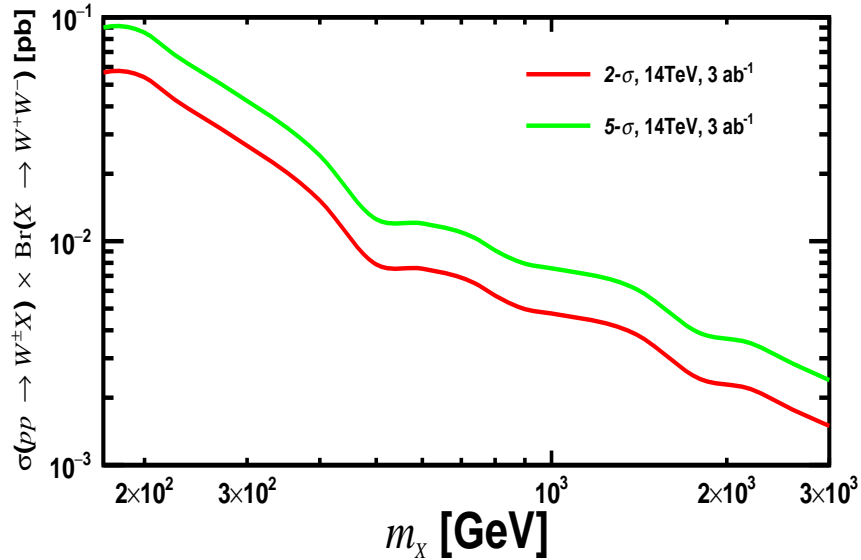


Figure 4: Discovery sensitivities on the production cross section $\sigma(pp \rightarrow W^\pm X)$ times branching ratio $\text{Br}(X \rightarrow W^+ W^-)$ in the mass range of 170 - 3000 GeV at the HL-LHC with $\sqrt{s} = 14$ TeV and $\mathcal{L} = 3 \text{ ab}^{-1}$. Red and green curves correspond to 2- σ and 5- σ significances, respectively.

In Fig. 5, for the concrete case of heavy photophobic ALPs, we show the discovery sensitivities on the coupling g_{aWW} with 2- σ and 5- σ significances as a function of the ALP mass m_a in the range of 170–3000 GeV at the HL-LHC, with $\sqrt{s} = 14$ TeV and integrated luminosities of 3 ab^{-1} and 35.9 fb^{-1} . For comparison, we also display the 95% C.L. limit (blue curve) from Ref. [44] which is derived from reinterpreting the CMS analyses

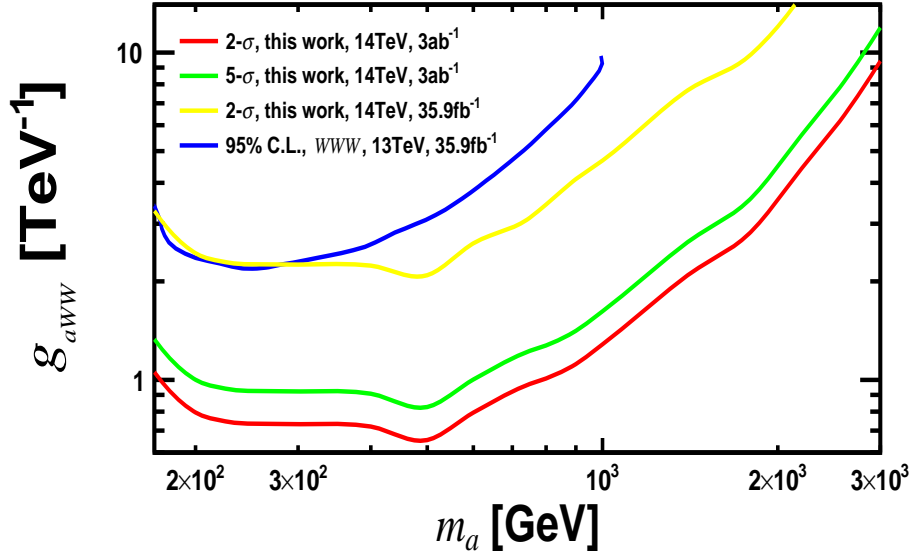


Figure 5: Discovery sensitivities with 2- σ and 5- σ significances on the coupling g_{aWW} in the mass range of 170 - 3000 GeV at the HL-LHC with $\sqrt{s} = 14$ TeV and $\mathcal{L} = 3 \text{ ab}^{-1}$ and 35.9 fb^{-1} . The 95% C.L. limit (blue curve) [44] derived from reinterpreting CMS analyses of SM production $pp \rightarrow W^\pm W^\pm W^\mp$ at $\sqrt{s} = 13$ TeV and $\mathcal{L} = 35.9 \text{ fb}^{-1}$ is displayed for comparison.

of the SM production $pp \rightarrow W^\pm W^\pm W^\mp$ at $\sqrt{s} = 13$ TeV with $\mathcal{L} = 35.9 \text{ fb}^{-1}$. Our results demonstrate that at the HL-LHC with $\mathcal{L} = 3 \text{ ab}^{-1}$, the 2- σ sensitivity for g_{aWW} decreases from 1.06 TeV^{-1} to 0.75 TeV^{-1} as m_a increases from 170 GeV to 225 GeV, remains nearly stable for m_a in the range of 225–600 GeV, and then rises sharply to 9.42 TeV^{-1} at $m_a = 3000$ GeV. This pattern reflects the varying sensitivity of the search strategy across different mass ranges.

One observes that with the same luminosity of 35.9 fb^{-1} , our strategy achieves better sensitivities for m_a above 300 GeV compared to the referenced approach [44]. This improvement is primarily due to differences in the optimization of the analysis strategies. The referenced studies focus on the SM process $pp \rightarrow W^\pm W^\pm W^\mp$, while our strategy is specifically tailored to the tri- W final state produced by a heavy resonance. For larger masses, the kinematics of these two processes differ significantly, allowing our approach to reject background more effectively, as demonstrated by the BDT distributions in Appendix C.

7 Conclusion

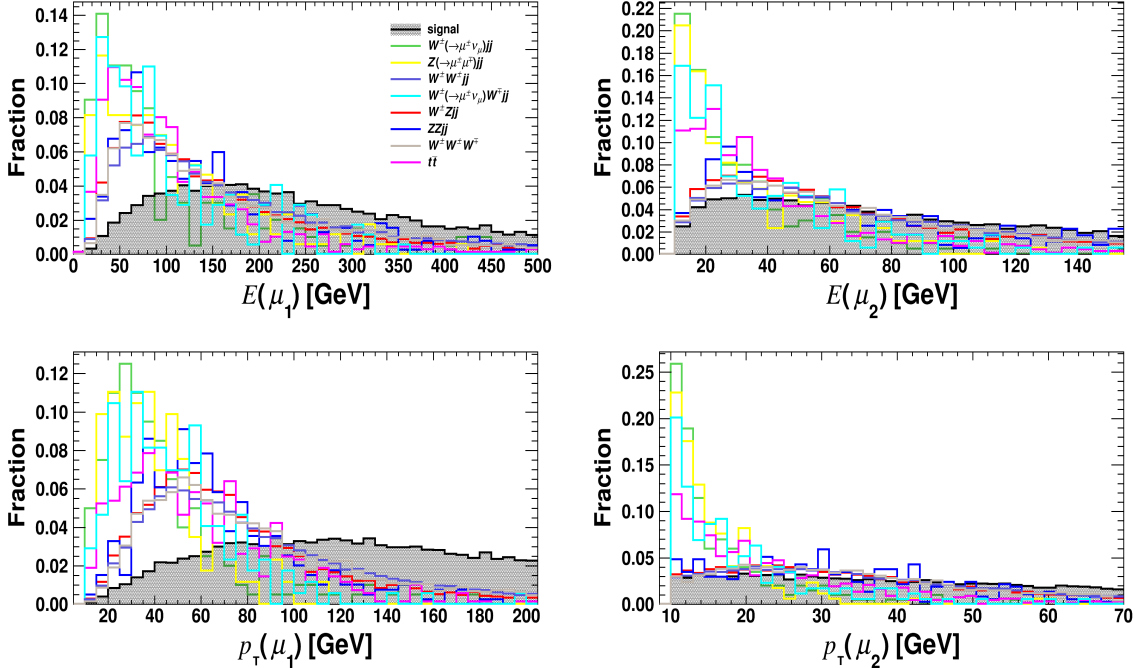
In this study, we proposed a search strategy at the HL-LHC for a new neutral particle X that couples to a pair of W -bosons. The particle X is produced with a W -boson and decays into two W -bosons, resulting in the process $pp \rightarrow W^\pm X (\rightarrow W^+ W^-)$ and a tri- W -boson final state. To suppress background, we focus on events where two same-charge W -bosons decay leptonically into muons, producing same-sign muons in the final state. The third

W -boson decays hadronically into jets, leveraging its higher branching ratio to enhance the signal. As a case study, we use the heavy photophobic ALP as an example.

Signal and background events are simulated at the detector level. The signal production cross section times branching ratio, $\sigma(pp \rightarrow W^\pm a) \times \text{Br}(a \rightarrow W^+W^-)$, is evaluated as a function of the ALP mass m_a at the HL-LHC with $\sqrt{s} = 14$ TeV. Events are selected with exactly two same-sign di-muons and at least two non- b -tagged jets. A machine-learning-based MVA is applied to enhance signal-background discrimination. Distributions of key input variables and the corresponding BDT responses are presented, and selection efficiencies for both preselection and BDT criteria are provided for various ALP masses.

We present the model-independent discovery sensitivities for the production cross section times branching ratio $\sigma(pp \rightarrow W^\pm X) \times \text{Br}(X \rightarrow W^+W^-)$ as a function of the particle mass m_X in the range of 170–3000 GeV at the HL-LHC with $\sqrt{s} = 14$ TeV and $\mathcal{L} = 3 \text{ ab}^{-1}$, which can be applied to general models involving a new neutral particle X that couples to W -bosons. The sensitivities for the coupling g_{aWW} of heavy photophobic ALPs are also shown for 2- σ and 5- σ significances in the same mass range under luminosities of 3 ab^{-1} and 35.9 fb^{-1} . At $\mathcal{L} = 3 \text{ ab}^{-1}$, the 2- σ sensitivity for g_{aWW} decreases from 1.06 TeV^{-1} to 0.75 TeV^{-1} as m_a increases from 170 GeV to 225 GeV, remains nearly constant for m_a between 225 and 600 GeV, and then sharply rises to 9.42 TeV^{-1} at $m_a = 3000$ GeV. Compared to previous limits derived from reinterpreting CMS analyses of SM production $pp \rightarrow W^\pm W^\pm W^\mp$ at $\sqrt{s} = 13$ TeV, our strategy provides improved sensitivity for m_a above 300 GeV.

A Distributions of Representative Observables



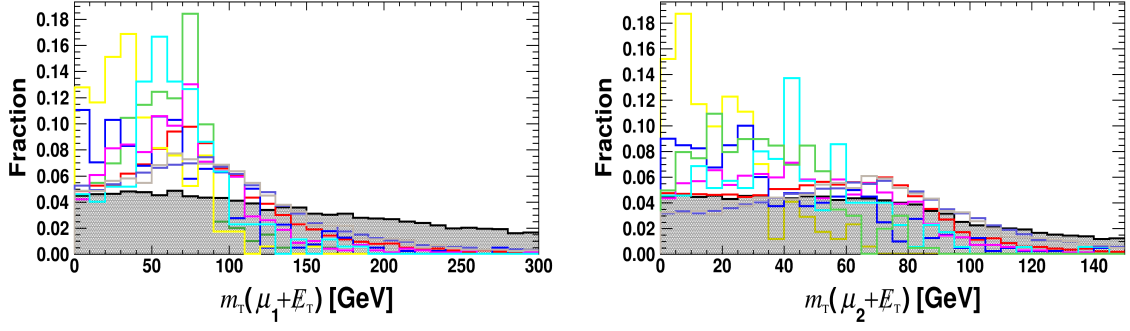
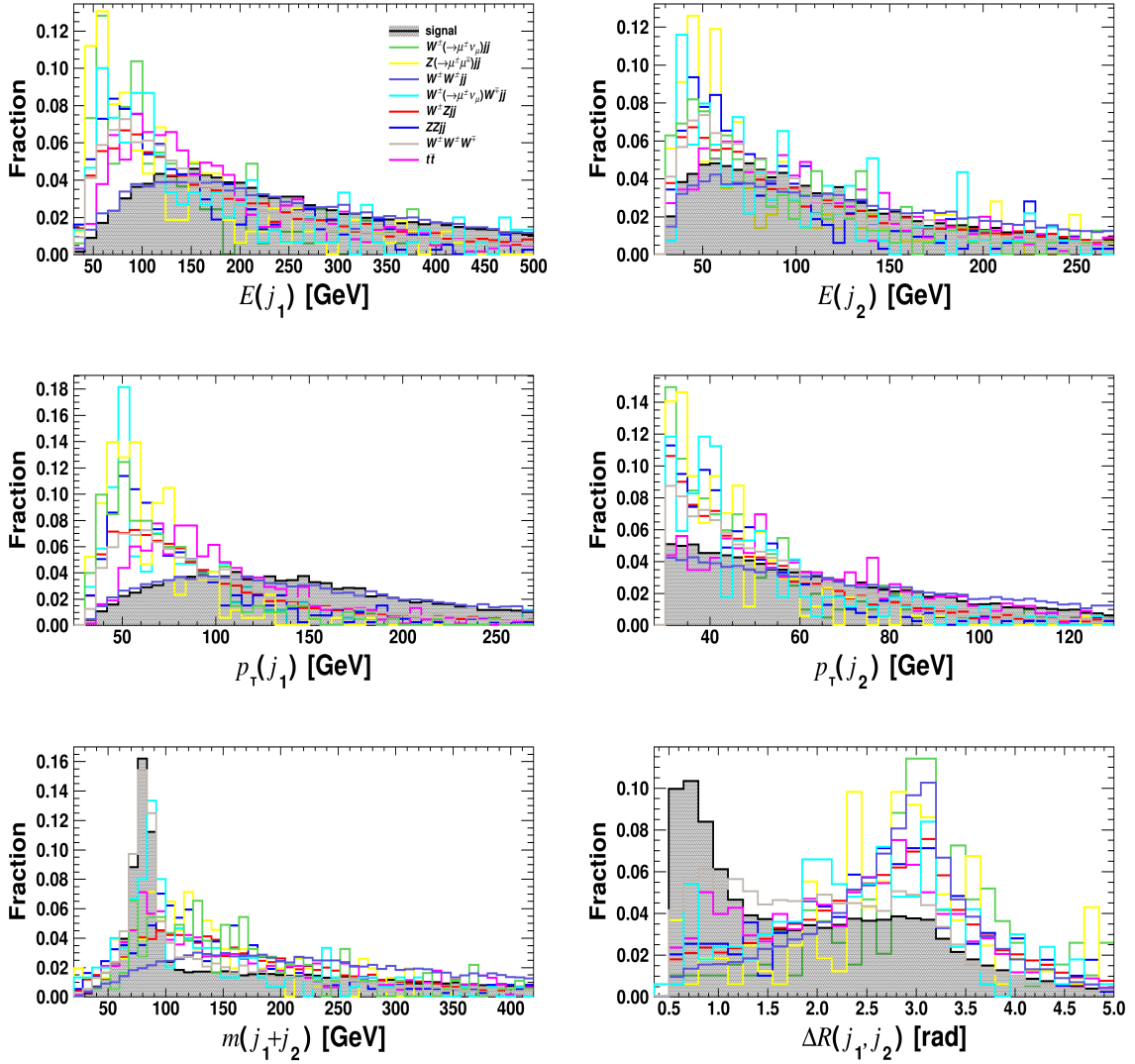


Figure 6: Distributions of kinematical observables for μ_1 and μ_2 after applying preselection criteria for the signal(black, shadow) and background processes at the HL-LHC with $\sqrt{s} = 14$ TeV, assuming the benchmark $m_a = 400$ GeV.



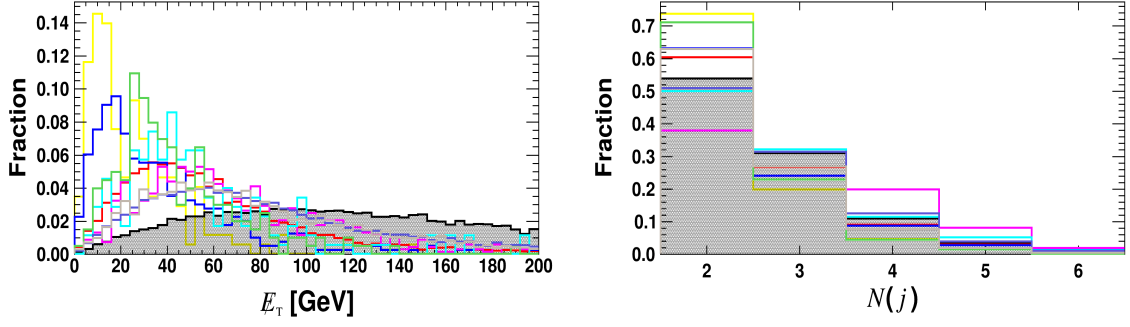


Figure 7: The same as Fig. 6, but for j_1 , j_2 , E_T and $N(j)$, assuming the benchmark $m_a = 400$ GeV.

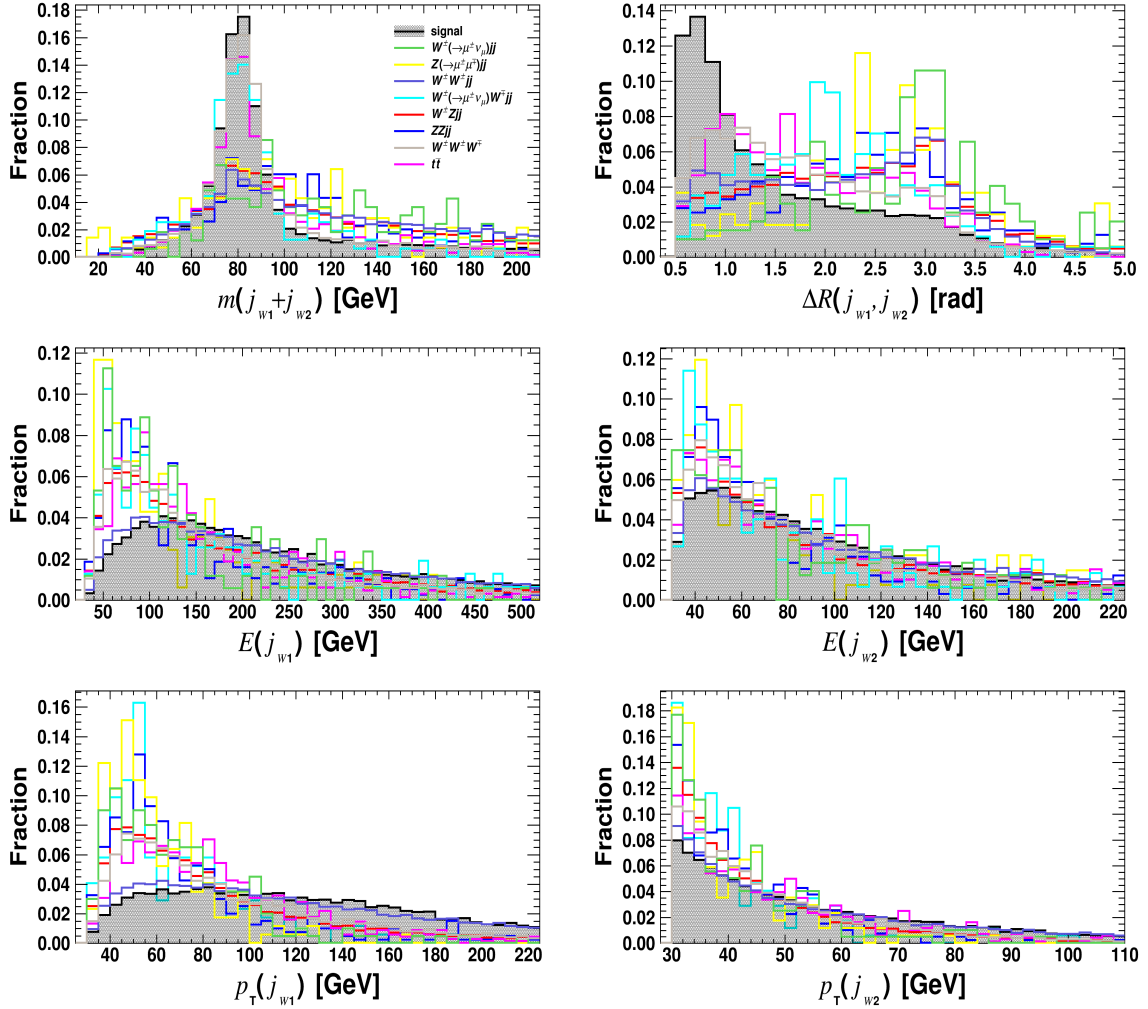


Figure 8: The same as Fig. 6, but for j_{w1} and j_{w2} , assuming the benchmark $m_a = 400$ GeV.

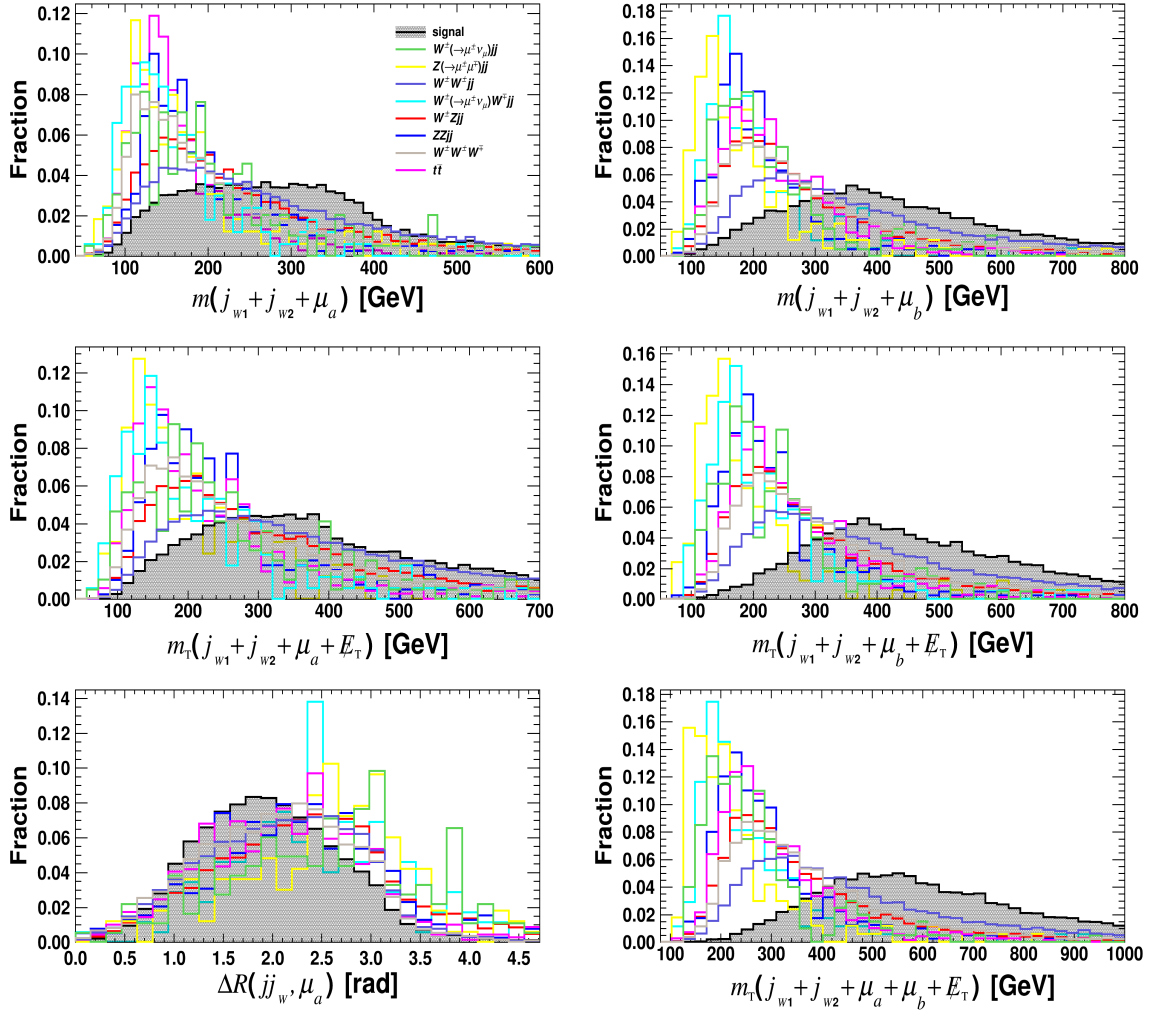
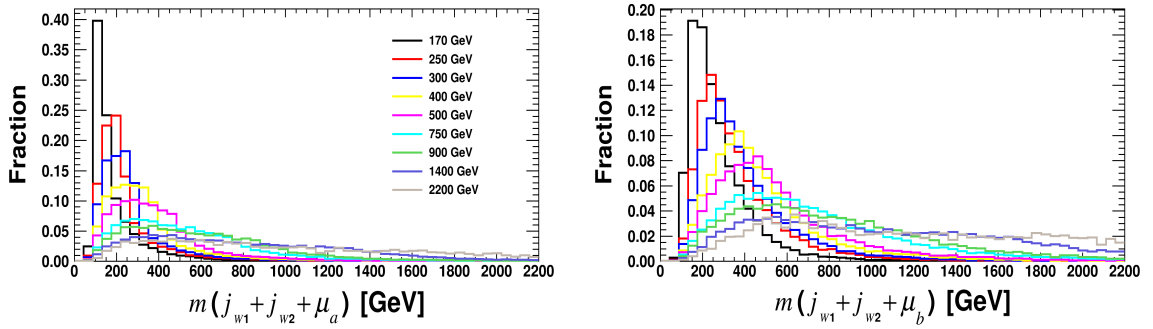


Figure 9: The same as Fig. 6, but for observables related to the reconstruction of the ALP mass and the off-shell $W^{(*)\pm}$ boson, assuming the benchmark $m_a = 400$ GeV.



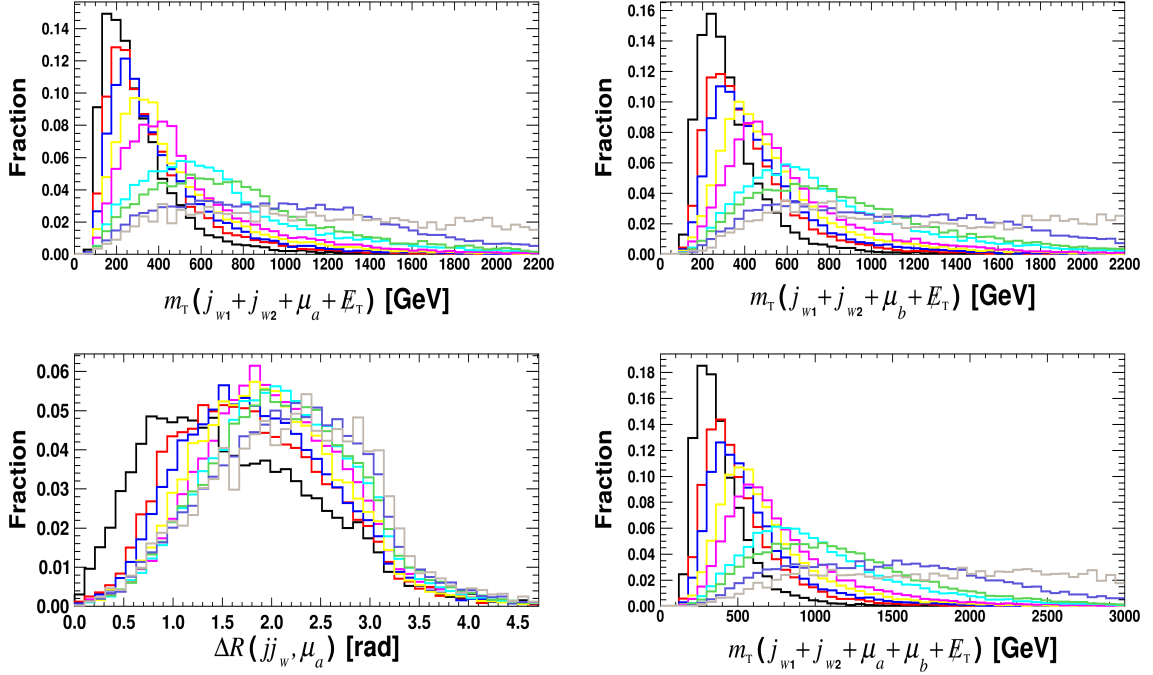


Figure 10: Distributions of same observables as Fig. 9, but for the signal only assuming different m_a values.

B Details of the MVA analyses

In this appendix, we provide detailed information about the MVA analyses performed using the TMVA package [56]. Fig. 11 illustrates the importance values of input observables as a

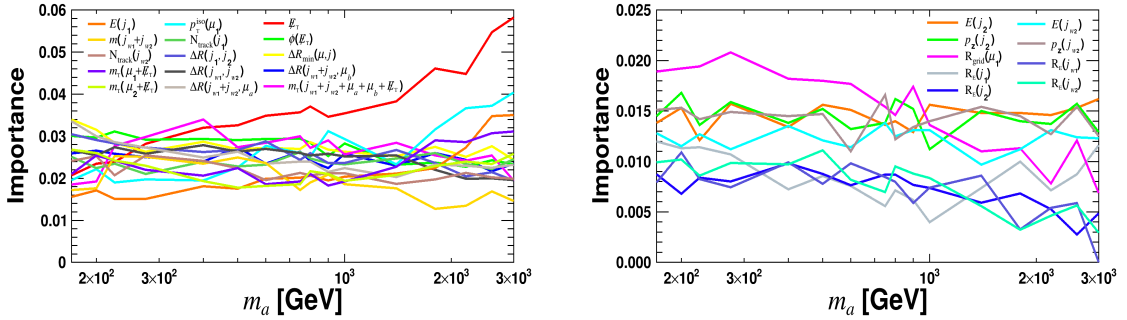


Figure 11: The importance values of input observables as a function of m_a , evaluated during the MVA training.

function of m_a , evaluated during the MVA training. The importance values for BDT input variables are quantified by counting how often the variables are used to split decision tree nodes, and by weighting each split occurrence by the separation gain-squared it has achieved and by the number of events in the node [56, 59]. The left plot highlights observables with

the highest importance values, while those with the lowest importance values are displayed in the right panel.

Table 2 presents the correlations between two observables for the total background and the signal with a benchmark mass $m_a = 400$ GeV. The listed 12 pairs have strong correlations and remain stable under variations of m_a . Fig. 12 displays the correlations

observables	signal	background
$p_T^{\text{iso}}(\mu_1)$, $p_{T,\text{max}}^{\text{iso}}(\mu)$	1.000	0.998
$m_T(j_{W1} + j_{W2} + \mu_b + \cancel{E}_T)$, $m_T(j_{W1} + j_{W2} + \mu_a + \mu_b + \cancel{E}_T)$	0.919	0.974
$m(j_{W1} + j_{W2} + \mu_b)$, $m_T(j_{W1} + j_{W2} + \mu_a + \mu_b + \cancel{E}_T)$	0.797	0.955
$m(j_{W1} + j_{W2} + \mu_a)$, $m(j_{W1} + j_{W2})$	0.845	0.865
$R_E(j_1)$, $R_E(j_{W1})$	0.762	0.896
$E(j_1)$, $E(j_{W1})$	0.747	0.850
$m(j_{W1} + j_{W2} + \mu_b)$, $m_T(j_{W1} + j_{W2} + \mu_b + \cancel{E}_T)$	0.724	0.926
$m(j_{W1} + j_{W2} + \mu_b)$, $m(j_{W1} + j_{W2})$	0.710	0.873
$m_T(j_{W1} + j_{W2} + \mu_b + \cancel{E}_T)$, $m(j_{W1} + j_{W2})$	0.715	0.861
$p_z(j_1)$, $p_z(j_{W1})$	0.791	0.838
$m(j_{W1} + j_{W2} + \mu_b)$, $m(j_{W1} + j_{W2} + \mu_a)$	0.740	0.861
$N_{\text{track}}(j_1)$, $N_{\text{track}}(j_{W1})$	0.761	0.772

Table 2: The correlations between two observables for the total background and the signal with a benchmark mass $m_a = 400$ GeV.

between pairs of observables for the signal as a function of m_a . The correlations for the selected pairs exhibit significant dependence on m_a .

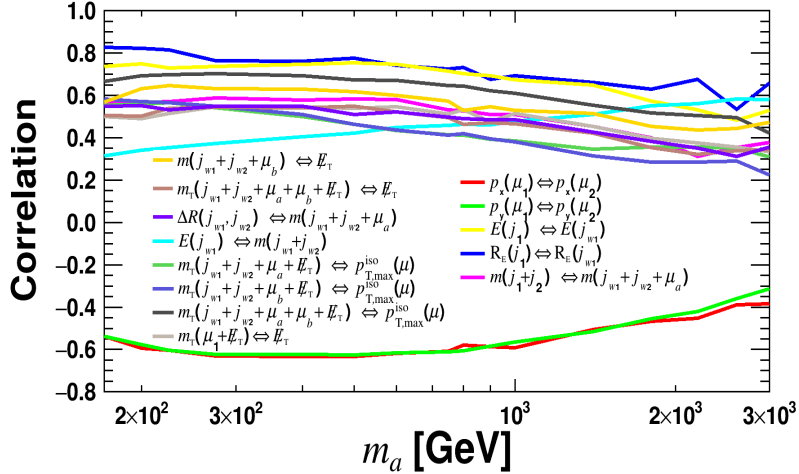


Figure 12: The correlations between pairs of observables for the signal as a function of m_a .

C Distributions of BDT responses

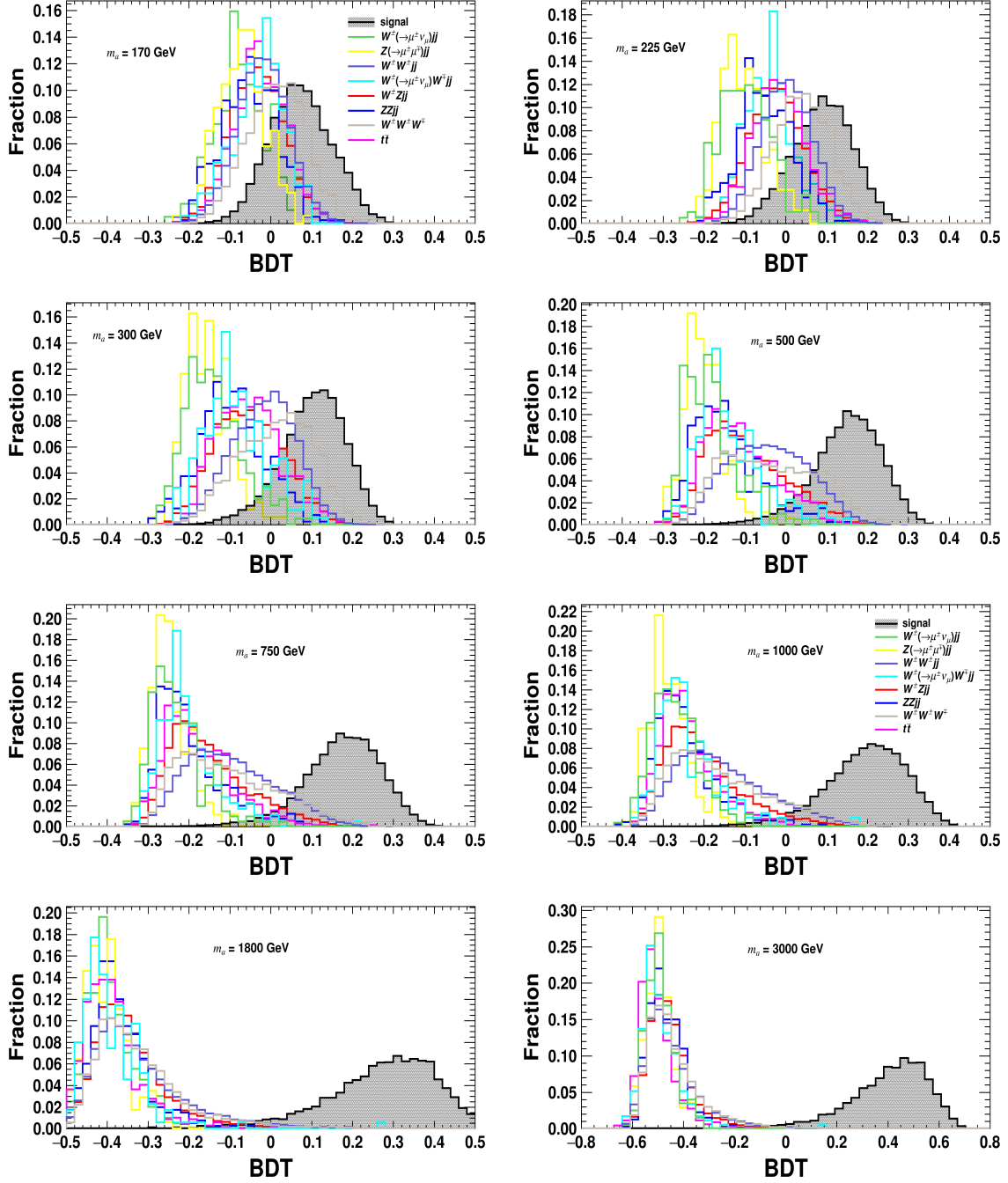


Figure 13: Distributions of BDT responses after applying preselection criteria for the signal (black, shadow) and background processes at the HL-LHC with $\sqrt{s} = 14$ TeV in representative m_a cases.

D The Selection Efficiency Table

m_a	selection	signal	$W^\pm Z jj$	$ZZ jj$	$Z(\rightarrow \mu^\pm \mu^\mp) jj$	$t\bar{t}$	$W^\pm(\rightarrow \mu^\pm \nu_\mu) W^\mp jj$	$W^\pm(\rightarrow \mu^\pm \nu_\mu) jj$	$W^\pm W^\pm jj$	$W^\pm W^\pm W^\mp$
170 GeV	preselection	2.18×10^{-3}	1.93×10^{-4}	5.00×10^{-5}	2.01×10^{-6}	1.63×10^{-5}	8.97×10^{-6}	1.35×10^{-6}	3.53×10^{-3}	2.26×10^{-3}
	BDT>0.127	2.46×10^{-1}	8.06×10^{-3}	7.50×10^{-3}	—	5.76×10^{-3}	—	—	1.08×10^{-2}	5.61×10^{-2}
200 GeV	preselection	2.79×10^{-3}	1.93×10^{-4}	5.00×10^{-5}	2.01×10^{-6}	1.63×10^{-5}	8.97×10^{-6}	1.35×10^{-6}	3.53×10^{-3}	2.26×10^{-3}
	BDT>0.108	4.15×10^{-1}	3.93×10^{-2}	1.50×10^{-2}	—	2.74×10^{-2}	1.14×10^{-2}	—	5.77×10^{-2}	1.86×10^{-1}
225 GeV	preselection	3.24×10^{-3}	1.93×10^{-4}	5.00×10^{-5}	2.01×10^{-6}	1.63×10^{-5}	8.97×10^{-6}	1.35×10^{-6}	3.53×10^{-3}	2.26×10^{-3}
	BDT>0.101	4.54×10^{-1}	3.70×10^{-2}	7.50×10^{-3}	—	4.61×10^{-2}	1.71×10^{-2}	—	5.63×10^{-2}	1.91×10^{-1}
275 GeV	preselection	3.76×10^{-3}	1.93×10^{-4}	5.00×10^{-5}	2.01×10^{-6}	1.63×10^{-5}	8.97×10^{-6}	1.35×10^{-6}	3.53×10^{-3}	2.26×10^{-3}
	BDT>0.115	4.79×10^{-1}	3.04×10^{-2}	1.00×10^{-2}	—	1.59×10^{-2}	5.71×10^{-3}	—	4.95×10^{-2}	1.66×10^{-1}
400 GeV	preselection	4.40×10^{-3}	1.93×10^{-4}	5.00×10^{-5}	2.01×10^{-6}	1.63×10^{-5}	8.97×10^{-6}	1.35×10^{-6}	3.53×10^{-3}	2.26×10^{-3}
	BDT>0.136	4.99×10^{-1}	1.12×10^{-2}	—	—	5.76×10^{-3}	—	—	2.49×10^{-2}	8.76×10^{-2}
500 GeV	preselection	4.61×10^{-3}	1.93×10^{-4}	5.00×10^{-5}	2.01×10^{-6}	1.63×10^{-5}	8.97×10^{-6}	1.35×10^{-6}	3.53×10^{-3}	2.26×10^{-3}
	BDT>0.165	5.38×10^{-1}	3.60×10^{-3}	—	—	1.44×10^{-3}	—	—	1.20×10^{-2}	3.49×10^{-2}
600 GeV	preselection	4.71×10^{-3}	1.93×10^{-4}	5.00×10^{-5}	2.01×10^{-6}	1.63×10^{-5}	8.97×10^{-6}	1.35×10^{-6}	3.53×10^{-3}	2.26×10^{-3}
	BDT>0.173	4.72×10^{-1}	2.45×10^{-3}	—	—	1.44×10^{-3}	1.14×10^{-2}	—	7.13×10^{-3}	2.54×10^{-2}
750 GeV	preselection	4.64×10^{-3}	1.93×10^{-4}	5.00×10^{-5}	2.01×10^{-6}	1.63×10^{-5}	8.97×10^{-6}	1.35×10^{-6}	3.53×10^{-3}	2.26×10^{-3}
	BDT>0.167	5.68×10^{-1}	2.02×10^{-3}	—	—	1.44×10^{-3}	1.14×10^{-2}	—	9.64×10^{-3}	2.04×10^{-2}
800 GeV	preselection	4.77×10^{-3}	1.93×10^{-4}	5.00×10^{-5}	2.01×10^{-6}	1.63×10^{-5}	8.97×10^{-6}	1.35×10^{-6}	3.53×10^{-3}	2.26×10^{-3}
	BDT>0.165	7.17×10^{-1}	3.46×10^{-3}	—	—	1.44×10^{-3}	1.14×10^{-2}	—	1.00×10^{-2}	2.02×10^{-2}
900 GeV	preselection	4.70×10^{-3}	1.93×10^{-4}	5.00×10^{-5}	2.01×10^{-6}	1.63×10^{-5}	8.97×10^{-6}	1.35×10^{-6}	3.53×10^{-3}	2.26×10^{-3}
	BDT>0.180	5.68×10^{-1}	1.44×10^{-3}	—	—	1.44×10^{-3}	5.71×10^{-3}	—	5.01×10^{-3}	1.01×10^{-2}
1000 GeV	preselection	4.72×10^{-3}	1.93×10^{-4}	5.00×10^{-5}	2.01×10^{-6}	1.63×10^{-5}	8.97×10^{-6}	1.35×10^{-6}	3.53×10^{-3}	2.26×10^{-3}
	BDT>0.140	8.69×10^{-1}	3.17×10^{-3}	—	—	2.88×10^{-3}	1.14×10^{-2}	—	1.35×10^{-2}	1.80×10^{-2}
1400 GeV	preselection	4.77×10^{-3}	1.93×10^{-4}	5.00×10^{-5}	2.01×10^{-6}	1.63×10^{-5}	8.97×10^{-6}	1.35×10^{-6}	3.53×10^{-3}	2.26×10^{-3}
	BDT>0.150	8.36×10^{-1}	2.02×10^{-3}	—	—	1.44×10^{-3}	5.71×10^{-3}	—	8.17×10^{-3}	9.11×10^{-3}
1800 GeV	preselection	4.78×10^{-3}	1.93×10^{-4}	5.00×10^{-5}	2.01×10^{-6}	1.63×10^{-5}	8.97×10^{-6}	1.35×10^{-6}	3.53×10^{-3}	2.26×10^{-3}
	BDT>0.150	8.31×10^{-1}	5.76×10^{-4}	—	—	1.44×10^{-3}	5.71×10^{-3}	—	3.50×10^{-3}	3.20×10^{-3}
2200 GeV	preselection	4.67×10^{-3}	1.93×10^{-4}	5.00×10^{-5}	2.01×10^{-6}	1.63×10^{-5}	8.97×10^{-6}	1.35×10^{-6}	3.53×10^{-3}	2.26×10^{-3}
	BDT>0.080	9.27×10^{-1}	7.20×10^{-4}	—	—	—	5.71×10^{-3}	—	5.01×10^{-3}	3.20×10^{-3}
2600 GeV	preselection	4.68×10^{-3}	1.93×10^{-4}	5.00×10^{-5}	2.01×10^{-6}	1.63×10^{-5}	8.97×10^{-6}	1.35×10^{-6}	3.53×10^{-3}	2.26×10^{-3}
	BDT>0.004	9.34×10^{-1}	4.32×10^{-4}	—	—	—	5.71×10^{-3}	—	3.07×10^{-3}	2.22×10^{-3}
3000 GeV	preselection	4.61×10^{-3}	1.93×10^{-4}	5.00×10^{-5}	2.01×10^{-6}	1.63×10^{-5}	8.97×10^{-6}	1.35×10^{-6}	3.53×10^{-3}	2.26×10^{-3}
	BDT>0.003	9.69×10^{-1}	8.64×10^{-4}	—	—	—	5.71×10^{-3}	—	4.82×10^{-3}	5.17×10^{-3}

Table 3: Selection efficiencies of preselection and BDT criteria for signal and background processes at the HL-LHC with $\sqrt{s} = 14$ TeV assuming different ALP masses, where “—” means the number of events can be reduced to be negligible with $\mathcal{L} = 3 \text{ ab}^{-1}$.

Acknowledgments

We thank Bin Diao and Zilong Ding for helpful discussions. Y.N.M. and Y.X. are supported by the National Natural Science Foundation of China under grant no. 12205227. K.W. is supported by the National Natural Science Foundation of China under grant no. 11905162, the Excellent Young Talents Program of the Wuhan University of Technology under grant no. 40122102, and the research program of the Wuhan University of Technology under grant no. 2020IB024. The simulation and analysis work of this article was completed with the computational cluster provided by the Theoretical Physics Group at the Department of Physics, School of Physics and Mechanics, Wuhan University of Technology.

References

- [1] P. Langacker, *The Physics of Heavy Z' Gauge Bosons*, *Rev. Mod. Phys.* **81** (2009) 1199 [[0801.1345](#)].
- [2] G.C. Branco, P.M. Ferreira, L. Lavoura, M.N. Rebelo, M. Sher and J.P. Silva, *Theory and phenomenology of two-Higgs-doublet models*, *Phys. Rept.* **516** (2012) 1 [[1106.0034](#)].

- [3] A. Djouadi, *The Anatomy of electro-weak symmetry breaking. II. The Higgs bosons in the minimal supersymmetric model*, *Phys. Rept.* **459** (2008) 1 [[hep-ph/0503173](#)].
- [4] S. Bhattacharya, G. Coloretti, A. Crivellin, S.-E. Dahbi, Y. Fang, M. Kumar et al., *Growing Excesses of New Scalars at the Electroweak Scale*, [2306.17209](#).
- [5] R.D. Peccei and H.R. Quinn, *CP Conservation in the Presence of Instantons*, *Phys. Rev. Lett.* **38** (1977) 1440.
- [6] R.D. Peccei and H.R. Quinn, *Constraints Imposed by CP Conservation in the Presence of Instantons*, *Phys. Rev. D* **16** (1977) 1791.
- [7] S. Weinberg, *A New Light Boson?*, *Phys. Rev. Lett.* **40** (1978) 223.
- [8] F. Wilczek, *Problem of Strong P and T Invariance in the Presence of Instantons*, *Phys. Rev. Lett.* **40** (1978) 279.
- [9] J.E. Kim and G. Carosi, *Axions and the Strong CP Problem*, *Rev. Mod. Phys.* **82** (2010) 557 [[0807.3125](#)].
- [10] G. Panico and A. Wulzer, *The Composite Nambu-Goldstone Higgs*, vol. 913, Springer (2016), [10.1007/978-3-319-22617-0](#), [[1506.01961](#)].
- [11] C. Csaki, M.L. Graesser and G.D. Kribs, *Radion dynamics and electroweak physics*, *Phys. Rev. D* **63** (2001) 065002 [[hep-th/0008151](#)].
- [12] F. Kahlhoefer, *Review of LHC Dark Matter Searches*, *Int. J. Mod. Phys. A* **32** (2017) [1730006](#) [[1702.02430](#)].
- [13] N. Craig, A. Hook and S. Kasko, *The Photophobic ALP*, *JHEP* **09** (2018) 028 [[1805.06538](#)].
- [14] M. Dine, *TASI lectures on the strong CP problem*, in *Theoretical Advanced Study Institute in Elementary Particle Physics (TASI 2000): Flavor Physics for the Millennium*, pp. 349–369, 6, 2000 [[hep-ph/0011376](#)].
- [15] J.E. Kim, *Weak Interaction Singlet and Strong CP Invariance*, *Phys. Rev. Lett.* **43** (1979) 103.
- [16] M.A. Shifman, A.I. Vainshtein and V.I. Zakharov, *Can Confinement Ensure Natural CP Invariance of Strong Interactions?*, *Nucl. Phys. B* **166** (1980) 493.
- [17] A.R. Zhitnitsky, *On Possible Suppression of the Axion Hadron Interactions. (In Russian)*, *Sov. J. Nucl. Phys.* **31** (1980) 260.
- [18] M. Dine, W. Fischler and M. Srednicki, *A Simple Solution to the Strong CP Problem with a Harmless Axion*, *Phys. Lett. B* **104** (1981) 199.
- [19] A. Hook, S. Kumar, Z. Liu and R. Sundrum, *High Quality QCD Axion and the LHC*, *Phys. Rev. Lett.* **124** (2020) 221801 [[1911.12364](#)].
- [20] J. Quevillon and C. Smith, *Axions are blind to anomalies*, *Eur. Phys. J. C* **79** (2019) 822 [[1903.12559](#)].
- [21] L. Di Luzio, M. Giannotti, E. Nardi and L. Visinelli, *The landscape of QCD axion models*, *Phys. Rept.* **870** (2020) 1 [[2003.01100](#)].
- [22] G. Galanti and M. Roncadelli, *Axion-like Particles Implications for High-Energy Astrophysics*, *Universe* **8** (2022) 253 [[2205.00940](#)].
- [23] K. Choi, S.H. Im and C. Sub Shin, *Recent Progress in the Physics of Axions and Axion-Like Particles*, *Ann. Rev. Nucl. Part. Sci.* **71** (2021) 225 [[2012.05029](#)].

- [24] Q. Qiu, Y. Gao, H.-j. Tian, K. Wang, Z. Wang and X.-M. Yang, *Wide Binary Evaporation by Dark Solitons: Implications from the GAIA Catalog*, [2404.18099](#).
- [25] M. Bauer, M. Neubert and A. Thamm, *Collider Probes of Axion-Like Particles*, *JHEP* **12** (2017) 044 [[1708.00443](#)].
- [26] M.J. Dolan, T. Ferber, C. Hearty, F. Kahlhoefer and K. Schmidt-Hoberg, *Revised constraints and Belle II sensitivity for visible and invisible axion-like particles*, *JHEP* **12** (2017) 094 [[1709.00009](#)].
- [27] M. Bauer, M. Heiles, M. Neubert and A. Thamm, *Axion-Like Particles at Future Colliders*, *Eur. Phys. J. C* **79** (2019) 74 [[1808.10323](#)].
- [28] H.-Y. Zhang, C.-X. Yue, Y.-C. Guo and S. Yang, *Searching for axionlike particles at future electron-positron colliders*, *Phys. Rev. D* **104** (2021) 096008 [[2103.05218](#)].
- [29] D. d’Enterria, *Collider constraints on axion-like particles*, in *Workshop on Feebly Interacting Particles*, 2, 2021 [[2102.08971](#)].
- [30] P. Agrawal et al., *Feebly-interacting particles: FIPs 2020 workshop report*, *Eur. Phys. J. C* **81** (2021) 1015 [[2102.12143](#)].
- [31] M. Tian, Z.S. Wang and K. Wang, *Search for long-lived axions with far detectors at future lepton colliders*, [2201.08960](#).
- [32] F.A. Ghebretinsaea, Z.S. Wang and K. Wang, *Probing axion-like particles coupling to gluons at the LHC*, *JHEP* **07** (2022) 070 [[2203.01734](#)].
- [33] C. Antel et al., *Feebly-interacting particles: FIPs 2022 Workshop Report*, *Eur. Phys. J. C* **83** (2023) 1122 [[2305.01715](#)].
- [34] T. Biswas, *Probing the interactions of axion-like particles with electroweak bosons and the Higgs boson in the high energy regime at LHC*, *JHEP* **05** (2024) 081 [[2312.05992](#)].
- [35] Y. Lu, Y.-n. Mao, K. Wang and Z.S. Wang, *LAYCAST: LAYered CAvern Surface Tracker at future electron-positron colliders*, [2406.05770](#).
- [36] PARTICLE DATA GROUP collaboration, *Review of particle physics*, *Phys. Rev. D* **110** (2024) 030001.
- [37] C. O’HARE, *cajohare/AxionLimits: AxionLimits*, <https://doi.org/10.5281/zenodo.3932429> (2024) .
- [38] BELLE-II collaboration, *Search for Axion-Like Particles produced in e^+e^- collisions at Belle II*, *Phys. Rev. Lett.* **125** (2020) 161806 [[2007.13071](#)].
- [39] BESIII collaboration, *Search for an axion-like particle in radiative J/ψ decays*, *Phys. Lett. B* **838** (2023) 137698 [[2211.12699](#)].
- [40] BESIII collaboration, *ALPs searches at BESIII*, in *57th Rencontres de Moriond on Electroweak Interactions and Unified Theories*, 5, 2023 [[2305.08043](#)].
- [41] CMS collaboration, *Evidence for light-by-light scattering and searches for axion-like particles in ultraperipheral PbPb collisions at $\sqrt{s_{NN}} = 5.02$ TeV*, *Phys. Lett. B* **797** (2019) 134826 [[1810.04602](#)].
- [42] ATLAS collaboration, *Measurement of light-by-light scattering and search for axion-like particles with 2.2 nb^{-1} of Pb+Pb data with the ATLAS detector*, *JHEP* **03** (2021) 243 [[2008.05355](#)].

- [43] J. Bonilla, I. Brivio, J. Machado-Rodríguez and J.F. de Trocóniz, *Nonresonant searches for axion-like particles in vector boson scattering processes at the LHC*, *JHEP* **06** (2022) 113 [[2202.03450](#)].
- [44] M. Aiko, M. Endo and K. Fridell, *Heavy photophobic ALP at the LHC*, *JHEP* **06** (2024) 194 [[2401.13323](#)].
- [45] ATLAS collaboration, *Search for triboson $W^\pm W^\pm W^\mp$ production in pp collisions at $\sqrt{s} = 8$ TeV with the ATLAS detector*, *Eur. Phys. J. C* **77** (2017) 141 [[1610.05088](#)].
- [46] CMS collaboration, *Measurements of production cross sections of WZ and same-sign WW boson pairs in association with two jets in proton-proton collisions at $\sqrt{s} = 13$ TeV*, *Phys. Lett. B* **809** (2020) 135710 [[2005.01173](#)].
- [47] CMS collaboration, *Search for the production of $W^\pm W^\pm W^\mp$ events at $\sqrt{s} = 13$ TeV*, *Phys. Rev. D* **100** (2019) 012004 [[1905.04246](#)].
- [48] Z. Ding, Y.-n. Mao and K. Wang, *Search for the γZ decay mode of heavy photophobic axion-like particles at the LHC*, [2411.08660](#).
- [49] M. Aiko and M. Endo, *Electroweak precision test of axion-like particles*, *JHEP* **05** (2023) 147 [[2302.11377](#)].
- [50] I. Brivio, M.B. Gavela, L. Merlo, K. Mimasu, J.M. No, R. del Rey et al., *ALPs Effective Field Theory and Collider Signatures*, *Eur. Phys. J. C* **77** (2017) 572 [[1701.05379](#)].
- [51] J. Alwall, R. Frederix, S. Frixione, V. Hirschi, F. Maltoni, O. Mattelaer et al., *The automated computation of tree-level and next-to-leading order differential cross sections, and their matching to parton shower simulations*, *JHEP* **07** (2014) 079 [[1405.0301](#)].
- [52] R.D. Ball et al., *Parton distributions with LHC data*, *Nucl. Phys. B* **867** (2013) 244 [[1207.1303](#)].
- [53] T. Sjöstrand, S. Ask, J.R. Christiansen, R. Corke, N. Desai, P. Ilten et al., *An introduction to PYTHIA 8.2*, *Comput. Phys. Commun.* **191** (2015) 159 [[1410.3012](#)].
- [54] DELPHES 3 collaboration, *DELPHES 3, A modular framework for fast simulation of a generic collider experiment*, *JHEP* **02** (2014) 057 [[1307.6346](#)].
- [55] C. Degrande, C. Duhr, B. Fuks, D. Grellscheid, O. Mattelaer and T. Reiter, *UFO - The Universal FeynRules Output*, *Comput. Phys. Commun.* **183** (2012) 1201 [[1108.2040](#)].
- [56] TMVA collaboration, *TMVA - Toolkit for Multivariate Data Analysis*, [physics/0703039](#).
- [57] J. Thaler, <http://madgraph.phys.ucl.ac.be/Manual/lhco.html>, .
- [58] T. Han, *Collider phenomenology: Basic knowledge and techniques*, in *Theoretical Advanced Study Institute in Elementary Particle Physics: Physics in $D \geq 4$* , pp. 407–454, 8, 2005, DOI [[hep-ph/0508097](#)].
- [59] L. Breiman, J. Friedman, R.A. Olshen and C.J. Stone, *Classification and Regression Trees*, Chapman and Hall/CRC (10, 2017), [10.1201/9781315139470](#).